



ELSEVIER

Available online at www.sciencedirect.com**ScienceDirect**journal homepage: www.elsevier.com/locate/ijrefrig

Small-scale turbocompressors for wide-range operation with large tip-clearances for a two-stage heat pump concept

Adeel Javed ^{a,*}, Cordin Arpagaus ^b, Stefan Bertsch ^b, Jürg Schiffmann ^a

^a Laboratory for Applied Mechanical Design (LAMD), École Polytechnique Fédérale de Lausanne (EPFL), Rue de la Maladière 71b, Neuchâtel 2002, Switzerland

^b Institute for Energy Systems, NTB University of Applied Sciences and Technology Buchs, Werdenbergstrasse 4, Buchs 9471, Switzerland

ARTICLE INFO

Article history:

Received 9 May 2016

Received in revised form 7 June 2016

Accepted 8 June 2016

Available online 14 June 2016

Keywords:

Two-stage heat pump

Small-scale turbocompressors

Two-zone meanline modeling

Tip-clearance effects

Optimum blade design

Computational fluid dynamics

(CFD)

ABSTRACT

Two mechanically driven small-scale turbocompressors running on gas lubricated bearings have been theoretically designed for a 6.5 kW two-stage heat pump functioning under variable operating conditions. The novelty in the heat pump system lies in the application of oil-free turbocompressor technology and the introduction of unused heat from various secondary heat sources. Managing the heat pump operational deviations with the secondary heat is difficult for the turbocompressors. The turbocompressors can potentially exceed their operating range defined by the surge, choke and maximum rotational speed margins. Furthermore, regulating the tip-leakage flow caused by large tip-clearances in small-scale turbomachinery is challenging. This paper will guide the readers through different stages of the design process of small-scale turbocompressors subjected to different operational and design constraints. The design review and the presented methodology will help the designers make suitable parameter selections for achieving high efficiency and wide compressor operating range.

© 2016 Elsevier Ltd and IIR. All rights reserved.

Turbocompresseurs de petite taille pour un fonctionnement sur une large plage avec des jeux radiaux importants pour un concept de pompe à chaleur bi-étagée

Mots clés : Pompe à chaleur bi-étagée ; Turbocompresseurs de petite taille ; Modélisation de la ligne moyenne de deux zones ; Effets des jeux radiaux ; Conception optimale d'aube ; Mécanique numérique des fluides (CFD)

URL: lamd.epfl.ch.

* Corresponding author. Laboratory for Applied Mechanical Design (LAMD), École Polytechnique Fédérale de Lausanne (EPFL), Rue de la Maladière 71b, Neuchâtel 2002, Switzerland.

E-mail address: adeel.javed@epfl.ch (A. Javed).

<http://dx.doi.org/10.1016/j.ijrefrig.2016.06.015>

0140-7007/© 2016 Elsevier Ltd and IIR. All rights reserved.

| Nomenclature | |
|---------------------|---|
| a | speed of sound [$m\ s^{-1}$] |
| A | area [mm^2] |
| b | height or width [mm] |
| c | absolute velocity/coefficient [$m\ s^{-1}/-$] |
| c_f | skin friction coefficient [–] |
| C_p | pressure recovery coefficient [–] |
| COP | coefficient of performance [–] |
| d | diameter [mm] |
| d_s | specific diameter [–] |
| DR | diffusion ratio [–] |
| i | incidence angle [deg] |
| k | relative surface roughness [–] |
| K | pressure loss coefficient [–] |
| \dot{m} | mass flow rate [$kg\ s^{-1}$] |
| M | Mach number [–] |
| n_s | specific speed [–] |
| N | rotational speed [min^{-1}] |
| p | pressure [Pa] |
| P | power [kW] |
| \dot{Q} | heat capacity [kW] |
| r | radius [mm] |
| R | range [–] |
| Re | Reynolds number [–] |
| SP | sizing parameter [–] |
| t | thickness/tip-clearance [mm/mm] |
| T | temperature [K] |
| u | blade speed [$m\ s^{-1}$] |
| w | relative velocity [$m\ s^{-1}$] |
| z | axial distance [mm] |
| α | absolute angle from the meridional axis [deg] |
| β | secondary heat fraction/relative angle from the meridional axis [–/deg] |
| χ | secondary mass flux fraction [–] |
| Δ | difference [%] |
| ε | relative tip-clearance [–] |
| η | efficiency [%] |
| λ | swirl parameter [–] |
| Λ | blade loading coefficient [–] |
| v | kinematic viscosity [$m^2\ s^{-1}$] |
| θ | wrap angle [deg] |
| ρ | density [$kg\ m^{-3}$] |
| Φ | global flow coefficient [–] |
| Π | pressure ratio [–] |
| ψ | azimuthal angle [deg] |
| Subscripts | |
| b | blade |
| c | critical, centroid |
| $cond$ | condenser |
| clr | clearance |
| des | design |
| $evap$ | evaporator |
| h | hub/hydraulic |
| int | intermediate |
| m | meridional/mixed-out |
| nd | non-dimensional |
| rel | relative |
| rot | rotor |
| sec | secondary |
| t | tip |
| vld | vaneless diffuser |
| vol | volute |
| θ | tangential |
| ψ | azimuthal angle |
| 0 | duct inlet/total condition |
| 1 | impeller inlet |
| 2 | impeller outlet |
| 5 | diffuser outlet |
| 6 | scroll outlet |
| 7 | volute outlet |
| Superscripts | |
| – | average or mean value |

1. Introduction

Heat pumps have been identified as a key technology for reducing exergy losses as compared to conventional boiler systems (Favrat et al., 2008). As the temperature levels are relatively low (about 30 °C to 60 °C), renewable energy sources can be utilized more effectively in place of fossil fuels. Heat pumps are not new; however, the technology has significantly evolved in terms of component and thermodynamic cycle efficiencies (Chua et al., 2010). One of the significant developments has been the realization of multi-stage heat pumps (Arpagaus et al., 2016; Bertsch and Groll, 2008; Favrat et al., 1997; Zehnder, 2004). Studies have shown that domestic-scale multi-stage heat pumps are feasible and achieve higher coefficient of performance (COP) values than single-stage types, but suffer from oil migration issues. Subsequently, a comprehensive design and experimental investigation of an oil-free gas bearing supported turbocompressor unit for a domestic two-stage heat

pump has been made (Schiffmann, 2013, 2015; Schiffmann and Favrat, 2009). The demonstrator turbocompressor with its 20 mm diameter centrifugal compressor wheel spinning over 200,000 min⁻¹ reached compressor isentropic and mechanical efficiencies of 80% and 95% mark, respectively, for R134a refrigerant fluid. The turbocompressor has seen application as a compressor-turbine unit in the experimental investigation of a thermally driven heat pump cycle with promising results (Demierre et al., 2014).

In this paper, a 6.5 kW two-stage heat pump concept driven by oil-free turbocompressors with two heat sources at different temperature levels is proposed for domestic applications. In addition to heat from the main source, a secondary heat from different unused sources such as waste heat, liquid from cooling circuits or process heat has been added to the thermodynamic cycle. It has been shown that additional heat input at higher temperature levels than the primary source has a benefit on the heat pump COP in heating mode (Granwehr and Bertsch, 2012). Fig. 1 illustrates the thermodynamic cycle of the two-

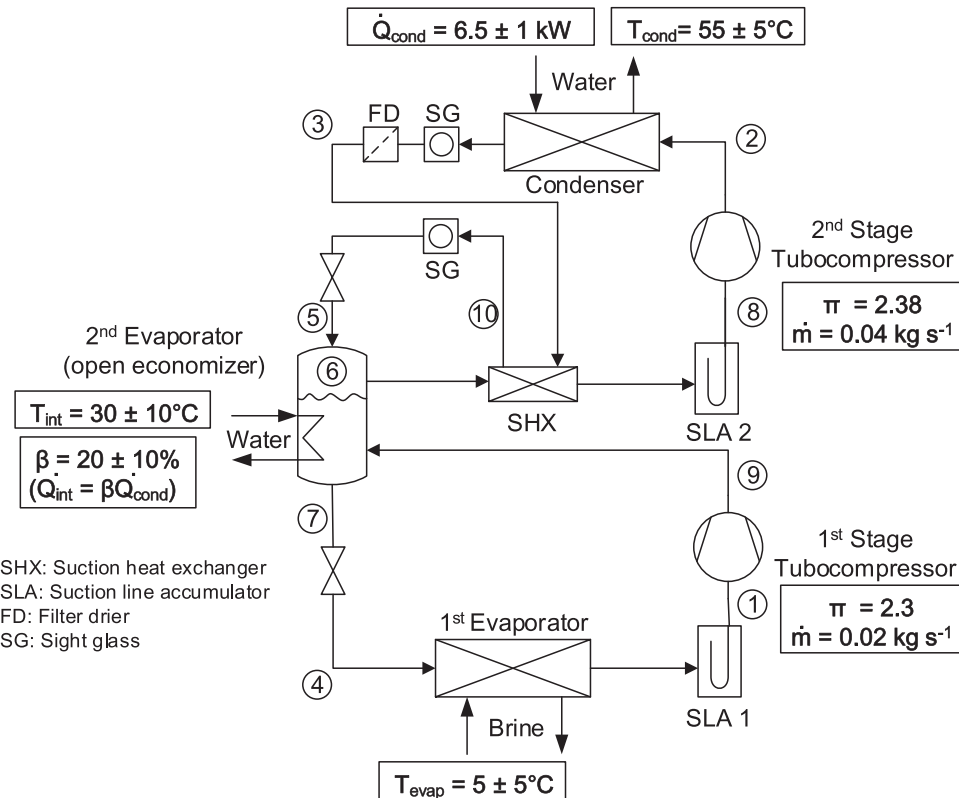


Fig. 1 – Schematic diagram of the two-stage heat pump cycle.

stage heat pump concept along with the operating conditions at various stations. The heat pump is designed for refrigerant fluid R134a to produce hot water at $T_{cond} = 55^\circ\text{C}$ for $\dot{Q}_{cond} = 6.5 \text{ kW}$ condenser heating capacity. The evaporator draws heat from brine at $T_{evap} = 5^\circ\text{C}$. Additionally, a second heat source \dot{Q}_{int} ranging from 10 to 30% β (where $\beta = \frac{\dot{Q}_{int}}{\dot{Q}_{cond}} \times 100\%$) at $T_{int} = 30^\circ\text{C}$ is introduced in the open economizer through a special integrated heat exchanger. This poses design challenges for the turbocompressors, especially in the first or low pressure stage since mass flow rate can fluctuate considerably depending on the β level for a constant condenser heating capacity and mass flow rate in the second or high pressure stage. For the given described design operating conditions and 20% β , the heat pump requires the design of first and second stage turbocompressors with 2.3 and 2.38 pressure ratios, and mass flow rates of 0.02 kg s^{-1} and 0.04 kg s^{-1} , respectively. Fig. 1 also details the possible temperature and power deviations during the heat pump operation. As the operating conditions of the heat pump deviate from the design point, the turbocompressors can potentially surge or choke depending on the magnitude of deviations. Hence, turbocompressors designed for wide operating range are required for this application.

1.1. Nature of the issues

The idea is to develop decentralized heat pump system with a low heat capacity in the condenser. This requires the design

of miniature turbocompressors. The main challenges faced by small-scale turbomachinery are: (1) high viscous losses due to low Reynolds number and large relative surface roughness, (2) manufacturing and assembly constraints resulting in large relative tip-clearance and thicker blades mainly, and (3) large heat flux from hot to cold sections due to shorter distances between components. For the present application, the surface roughness and tip-clearance are of prime concern during compressor design and development. Furthermore, there is no established design procedure available that could be applied to design such small-scale turbocompressors in a constrained design space.

1.2. Goals and objectives

The goal of this study is to achieve feasible turbocompressor designs by using a mix of one-dimensional (1D) and three-dimensional (3D) design methods. The foremost aim is to understand the complex relationship between many different geometric and fluid related parameters and make the most appropriate design selections, keeping in view the design requirement of having high compressor efficiency as well as a wide operating range. The main objectives are to: (1) review and summarize the design guidelines available in literature, (2) define the compressor specifications, (3) assess the effect of operational uncertainties on the compressor and heat pump performance, and (4) devise a unified guideline for optimum impeller blade design of small-scale compressors in the presence of large relative tip-clearance.

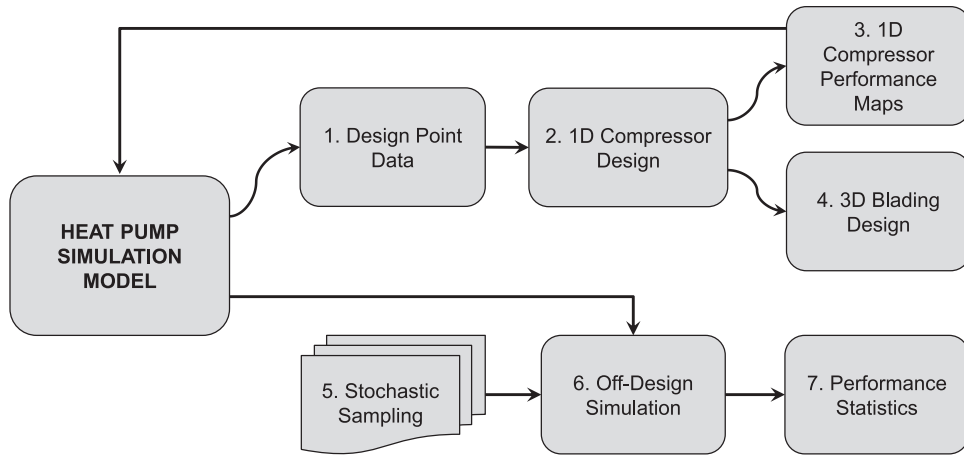


Fig. 2 – Methodology for turbocompressor design and heat pump simulation.

1.3. Scope of the paper

A comprehensive methodology has been applied to design the turbocompressors. Fig. 2 illustrates the different steps involved in the design process. The procedure begins with the heat pump modeling and simulation for the given set of operating conditions to obtain the design point specifications. For this, an in-house Matlab based model has been developed to calculate the steady-state performance of the two-stage heat pump concept. The model calls the real gas refrigerant database Refprop (Lemmon et al., 2002) to estimate the R134a refrigerant fluid properties. Subsequently, a 1D centrifugal compressor design has been made. The 1D design defines the preliminary geometry and performance maps of the two turbocompressor stages. The 1D maps are then integrated in the heat pump model to simulate off-design heat pump operation. A stochastic evaluation using Monte Carlo method has been made in order to determine the off-design heat pump and compressor performance statistics considering the different operational variables and their deviations. Finally, the 1D design is used to form a baseline 3D shape and blading optimization using comprehensive CFD modeling. The 3D blade passage design, and its influence on the compressor fluid physics is carefully studied.

2. 1D turbocompressor design

The turbocompressor design process begins with 1D meanline modeling of different components as illustrated in Fig. 3. A commercial 1D model COMPAL® from Concepts NREC has been used. The model is based on the two-zone methodology (Dean, 1974; Japikse, 1985, 1996). The design process begins at the inducer (station 1), proceeds to the exducer with primary and secondary zone calculations, and an effective mixed-out impeller exit station (station 2m), and then to the stationary components comprising a vaneless diffuser (station 5) and the discharge volute (station 6 and 7).

2.1. Design selections and review

A set of inputs is required during the design process. Selection of these inputs is based on designer's experience,

performance requirements and any design constraints. The selections made for the turbocompressor designs are detailed as follows:

Rotational speed selection. The $n_s d_s$ diagram for single stage compressors (Balje, 1981) has been used to obtain a conservative estimate of the turbocompressor rotational speed at design point. The maximum rotational speed and transmission torque are limited to $280,000 \text{ min}^{-1}$ and $45 \times 10^{-3} \text{ Nm}$, respectively. For the first stage turbocompressor, $n_s = 0.62$ has been selected, which complies with the 80% compressor efficiency island for a radial-type compressor. This results in an impeller with tip diameter of 15.2 mm and rotational speed of approximately $227,000 \text{ min}^{-1}$ at a torque of $21 \times 10^{-3} \text{ Nm}$. For the second stage turbocompressor, $n_s = 0.62$ would result in a design rotational speed of approximately $260,000 \text{ min}^{-1}$, leaving less speed margin for off-design heat pump operation. Therefore, a trade-off has been made by selecting a comparatively lower specific speed $n_s = 0.57$. Consequently, an impeller with tip diameter of 14.8 mm and rotational speed of approximately $235,000 \text{ min}^{-1}$ at a torque of $39 \times 10^{-3} \text{ Nm}$ is obtained.

Inducer design. Inducer forms the axial inlet section of the impeller. Preliminary sizing suggests that the global flow coefficient $\Phi = \dot{m}/\rho_0 u_2 d_2^2$ (Rusch and Casey, 2012) is in the moderate lower range of 0.04 to 0.05 for the particular turbocompressors. Inducer-less impellers having a blade with low aspect ratio are commonly designed for low values of Φ incurring relatively higher wall friction losses (Aungier, 2000; Lettieri et al., 2014). Nonetheless, an impeller designed with an inducer can give a larger throat area, thereby choking later than an inducer-less impeller as reported in Cumpsty (2004). Furthermore, shorter inducer-less impellers with higher curvature also exhibit greater acceleration of flow at the shroud causing a performance loss (Rusch and Casey, 2012; van den Braembussche, 2006). Therefore, an inducer has been included in the current impeller designs considering the possibility of achieving better performance and wider operating range. Typical design considerations for an inducer collected in the literature are summarized as follows:

- Hub-to-tip ratio r_{th}/r_{lt} (where r_{lt} includes blade tip radius and the tip-clearance gap) are defined in the range of 0.3

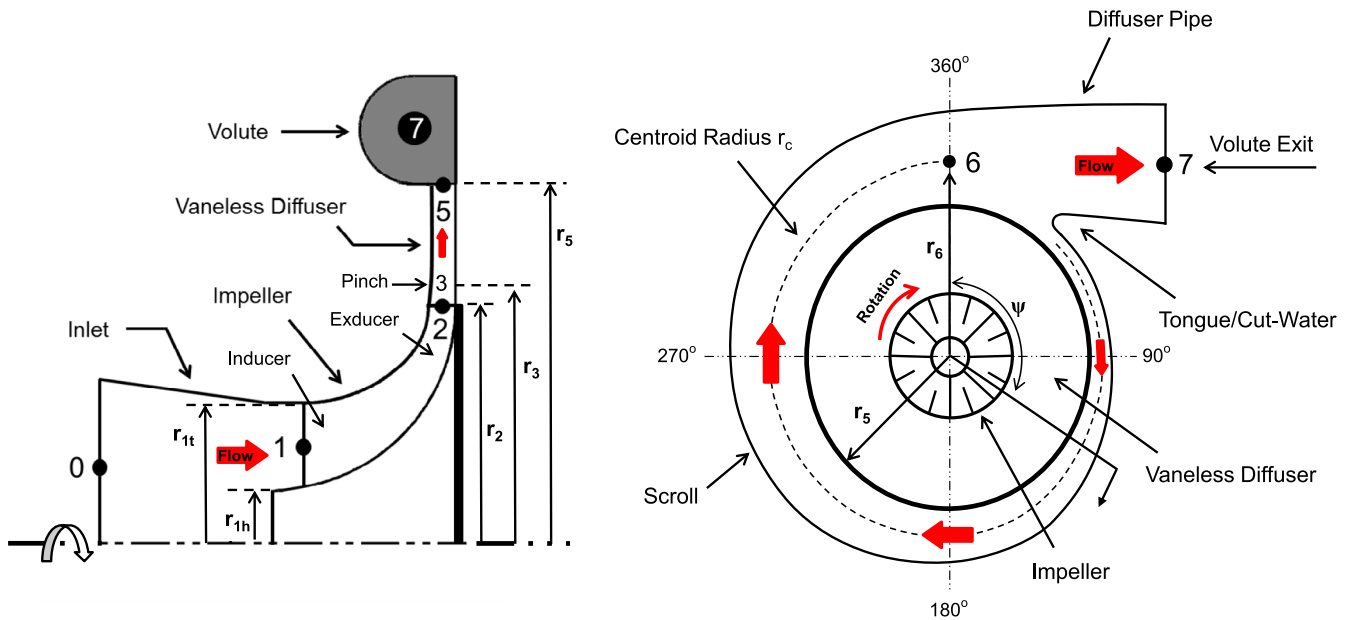


Fig. 3 – The centrifugal compressor stage and volute with station numbers and main dimensions.

to 0.5 with 0.7 as an upper limit (Japikse, 1996; van den Braembussche, 2007; Walsh and Fletcher, 2004). The actual hub size will depend on the number of blades (manufacturing and blockage constraints), the minimum shaft diameter required to transmit the torque (structural constraints), the rotordynamic aspects, and the inducer relative tip Mach number $M_{1t,rel}$ (Walsh and Fletcher, 2004; Whitfield and Baies, 1990).

- Hub radius ratio r_{1h}/r_2 is suggested to be in the range of 0.25 to 0.4 and can also be used to verify the optimum inducer hub radius r_{1h} (Casey, 2012).
- Tip radius ratio r_{1t}/r_2 is recommended to be between 0.5 and 0.8. This ratio influences the meridional curvature at impeller shroud from leading edge (LE) to the trailing edge (TE). A lower value would result in longer blade channels with somewhat larger friction. A higher value would cause a sharp meridional curvature; thus increasing the secondary flow losses, and less loss-free centrifugal effect ($u_2^2 - u_{1t}^2$) to diffuse the flow along the shroud (Cumpsty, 2004; Rusch and Casey, 2012; van den Braembussche, 2007).
- Relative tip Mach number $M_{1t,rel}$ is minimized for better diffusion in the impeller passage and less mixing loss downstream of the impeller. A shroud blade angle β_{1t} in the order of 55° to 60° is achieved accordingly (Aungier, 2000; Dixon, 2005; Rusch and Casey, 2012).

Focusing on the first stage turbocompressor only, a parametric study has been performed using the 1D design tool in order to determine the most appropriate inducer geometry. The inducer hub radius r_{1h} is sequentially increased from 1.5 mm to 3.0 mm and 1D calculations are made. Fig. 4 compares the variation of different dimensional ratios in relation to the impeller isentropic efficiency η_{rot} . Maximum impeller isentropic efficiency η_{rot} is obtained for the lowest r_{1h} . Impeller performance is improved mainly due to reduction in internal losses as optimum $M_{1t,rel} = 0.8$ for $r_{1h} = 3.0$ mm

is lowered to $M_{1t,rel} = 0.68$ for $r_{1h} = 1.5$ mm (also lower inducer tip radius r_{1t}). The diffusion properties are improved as the impeller with $r_{1h} = 1.5$ mm carries a lower overall diffusion ratio $DR = 1.56$ compared to $DR = 1.64$ for the impeller with $r_{1h} = 3.0$ mm (where $DR = w_{1t}/w_{2m}$). A higher choke margin is also expected, thus increasing the compressor operating range. The impeller will be mounted on a separate titanium shaft fused to the main rotor. Since the shaft can be designed independently of the main rotor and the torque transmission is well within the torsional rigidity limit, $r_{1h} = 1.5$ mm is finally selected for the turbocompressors. Interestingly, none of the parameters are meeting the optimum design rules, thus suggesting a review for low flow coefficient and refrigerant based turbocompressors. Finally, to delay inducer stall, an incidence angle of $i_{1t} = +1^\circ$ has been specified at the tip.

Number of blades, blade thickness and tip-clearance. A total of 16 blades have been specified for the turbocompressor impellers. Half of the blades are allocated to splitter blades, which can help in lowering the blade loading in the exducer and increase the inducer throat area; hence giving higher choke margin, and allow more space for a larger milling tool cut. The smallest manufacturable blade thickness t_b was limited to 0.2 mm. To be on the safe side, $t_b = 0.25$ mm is selected. The blades are non-tapered i.e., the blade thickness is uniformly distributed resulting in less blade blockage and improved performance. Aluminum is sufficient as material for impellers having tip speeds nearing 500 m s⁻¹ (Saravanamuttoo et al., 2001; Walsh and Fletcher, 2004). Due to low tip speeds in the range of 220 m s⁻¹, the turbocompressor impellers will be manufactured from aluminum. As centrifugal and thermal expansions are not expected at such low tip speeds, the tip-clearance t_{clr} is defined based on the manufacturing and assembly limitations, and bearing clearances only. A tip-clearance t_{clr} in the range of 50–80 μm is achievable for the turbocompressors. To begin with, $t_{clr} = 80 \mu\text{m}$ is selected with an intent to reduce it

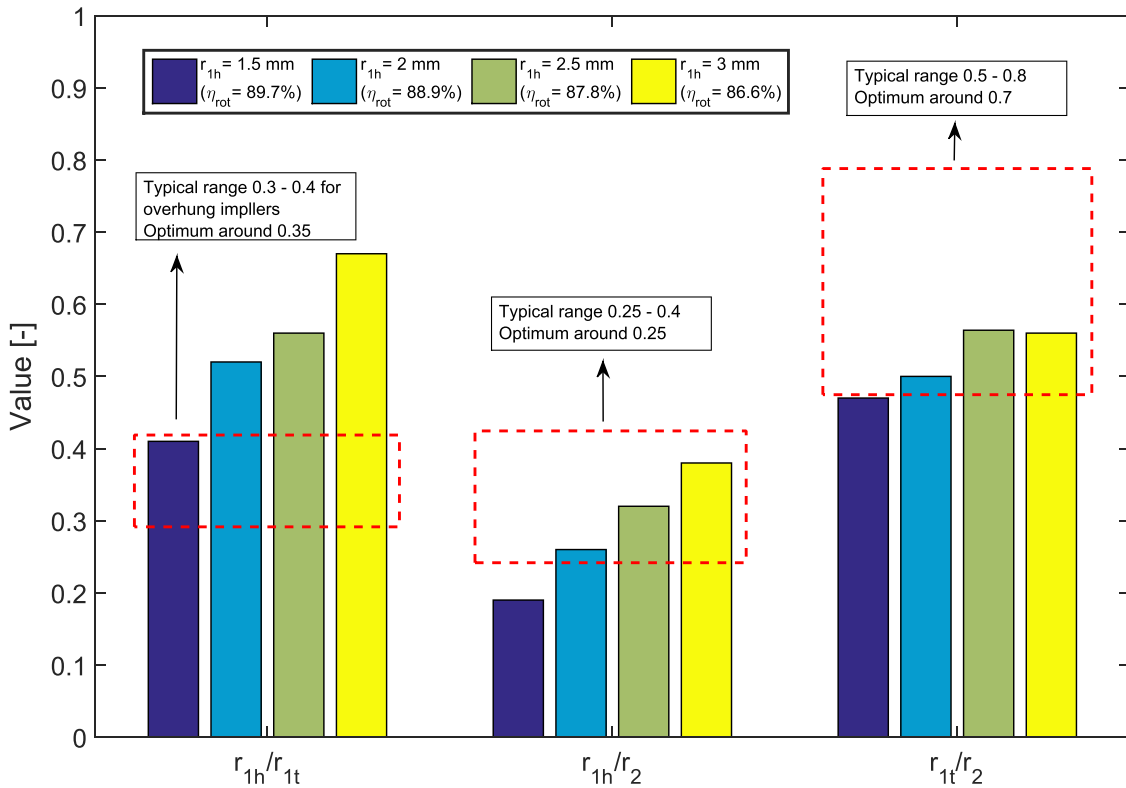


Fig. 4 – Parametric evaluation of inducer design for the first stage turbocompressor.

in the subsequent design phases and assess its effect on performance experimentally.

Exducer design. The two-zone modeling is case-specific in terms of computation of the mass flow distribution between the primary and secondary flow zones represented by the secondary zone mass flux fraction χ (where $\chi = \dot{m}_{\text{sec}}/\dot{m}$). Defining a constant χ is a conservative approach, which has been considered a modeling defect in Dean (1974). Relevant studies have been made to estimate the variation in χ for different compressor geometries and operating conditions (Hildebrandt and Genrup, 2007; Japikse, 1996; Javed, 2014; Javed et al., 2011). Since data are not available for small-scale impellers in the range of 15 mm tip diameter, a value $\chi = 0.2$ has been selected for the 1D designs.

The use of blade backsweep β_{2b} extends the compressor operating range, improves impeller exit flow uniformity, and increases the overall pressure recovery in the compressor (Gumpsty, 2004; Hildebrandt and Genrup, 2007; Japikse, 1996). On the other hand, a backswept impeller also reduces the swirl velocity $c_{\theta 2m}$ in the exducer, thus limiting the impeller work input, which has to be compensated by increasing the peripheral speed (either by increasing u_2 or r_2). Modern impeller designs can have a backsweep angle β_{2b} as high as 40° to 50° (Baines, 2005). For the turbocompressors, a $\beta_{2b} = 45^\circ$ has been selected.

To set the exducer depth or height b_2 for the turbocompressor impellers, the exit swirl parameter $\lambda_{2m} = c_{\theta 2m}/c_{m2m}$ has been defined, which gives a direct measure of the absolute flow angle α_{2m} (as $\alpha_{2m} = \tan^{-1}\lambda_{2m}$). In Japikse (1996), relevant guidelines are provided for an appropriate selection of λ_{2m} as a function of specific speed n_s .

Accordingly, the exit swirl parameter $\lambda_{2m} = 4.0$ ($\alpha_{2m} = 76^\circ$) and $\lambda_{2m} = 4.2$ ($\alpha_{2m} = 76.6^\circ$) have been specified for the first and second stage turbocompressors, respectively. The exducer is optimized in conjunction with the two-elements-in-series model (TEIS) (Japikse, 1984, 1996). Empirical parameters η_a and η_b are required, which represent the pressure recovery effectiveness or the quality of diffusion in the inducer and exducer sections, respectively. Following the guidelines provided in Japikse (1996) for small-scale impellers, $\eta_a = 0.4$ and $\eta_b = 0.2$ have been defined in the TEIS model for both turbocompressors. However, these are conservative estimates and are subjected to modifications once more diffusion data (CFD or experimental) becomes available for the particular turbocompressor cases.

Vaneless diffuser design. Although a vaneless diffuser can achieve higher peak efficiency, a vaneless diffuser has been selected for the turbocompressors due to the requirement of a wide operating range. For the impellers having the exit swirl parameter λ_{2m} in the range of 4.0 ($\alpha_{2m} \approx 76^\circ$) at the design point, the vaneless diffuser is likely to experience a rotating stall already, triggered by the local flow reversal in the diffuser. The critical diffuser inlet flow angle α_{2c} can be introduced here as a measure for predicting the onset of a flow reversal and an eventual diffuser rotating stall. Many theoretical and experimental studies have been performed to predict α_{2c} in relation to different influential factors – mainly the ratios b_2/r_2 and r_2/r_1 , inlet flow distortion, inlet Mach number and Reynolds number (Jansen, 1964; Otugen and So, 1988; Senoo and Kinoshita, 1977). Of all these factors, the ratio b_2/r_2 has the most significant effect on α_{2c} . With a reduction in b_2/r_2 , the critical flow angle α_{2c} increases, while reverse flow occurs closer to the diffuser inlet.

At condition $\alpha_{2m} \geq \alpha_{2c}$, the adverse pressure gradient and the shear stresses at the diffuser walls could force the near-wall boundary layer to overturn causing the local streamlines to reach angles above 90° (from the meridional direction) (Japikse, 1996). Furthermore, for highly swirling flows, the flow path in the vaneless space is also longer, thereby leading to higher frictional losses (Lettieri et al., 2014).

For wide-range and peak efficiency at design point, λ_{2m} should ideally be between approximately 2.0 and 2.5 (α_{2m} between 63° and 68°) (Jansen, 1964; Japikse, 1996; Johnston and Dean, 1966; Rodgers and Sapiro, 1972). Introducing a pinch downstream ($b_3/r_2 < b_2/r_2$) in the vaneless diffuser can increase the α_{2c} by locally increasing the meridional velocity c_{m2m} causing the swirl to decrease to a more desirable value for the diffuser ($\lambda_3 < \lambda_{2m}$). Furthermore, the diffuser pinch also weakens the tip-clearance sensitivity (Backman et al., 2007). The front pinch type has been applied in the turbocompressor vaneless diffusers. For the first stage turbocompressor, the front pinch reduces the exit height of the vaneless diffuser b_5 to 0.65 times the impeller exit height b_2 ($b_5/b_2 = 0.65$). Moreover, the diffuser exit radius r_5 has been maintained at 1.65 times the impeller exit radius r_2 ($r_5/r_2 = 1.65$). This causes $\lambda_{2m} = 4.0$ ($\alpha_{2m} = 76^\circ$) to drop to $\lambda_5 = 2.25$ ($\alpha_{2m} = 66^\circ$) at diffuser exit (assuming $\lambda_3 = \lambda_5$). Because operating range is not a critical requirement for the second stage turbocompressor, $\lambda_{2m} = 4.2$ ($\alpha_{2m} = 76.6^\circ$) has been reduced to $\lambda_5 = 2.9$ ($\alpha_{2m} = 71^\circ$) by introducing the front pinch. The pinch reduces the exit height of the vaneless diffuser b_5 to 0.8 times the impeller exit height b_2 ($b_5/b_2 = 0.8$), while the diffuser exit radius r_5 has been maintained at 1.65 times the impeller exit radius r_2 ($r_5/r_2 = 1.65$). The pinch is located at about 1.1 times the impeller exit radius r_2 ($r_3/r_2 = 1.1$). During detailed design, this allows a gradual and smooth transition from b_2 to b_3 , thus preventing a large increase in frictional losses with rapid increase in the radial velocity.

Volute design. An overhung external volute design with tunnel-type cross-sections has been opted for the turbocompressors due to its manufacturability by machining. The 1D meanline model features a semi-external volute design by default. Hence, the actual volute design has been made separately, while the 1D model data represents the default volute design. The cross-sectional areas A_ψ at different azimuth angles ψ have been sized following a simple correlation derived from the principles of angular momentum and mass conservation as $A_\psi = \psi \times SP \times \frac{r_c b_5}{\lambda_5}$. Here SP represents the sizing parameter used to scale the volute to account for the higher mean velocity than the ideal caused by the distorted profiles, viscous effects and secondary flows in the volute (Aungier, 2000).

In the present case, SP has also been used for maintaining an almost constant velocity ($c_{05} \approx c_6$) from diffuser exit to the scroll outlet. The external volute design causes the centroid radius at scroll exit r_6 to exceed the diffuser exit radius r_5 ($r_6 > r_5$), thus resulting in $c_{05} > c_6$ following the conservation of angular momentum, and eventually an unwanted diffusion at design point. Through an iterative procedure, $SP = 0.85$ has been found to be an appropriate scale for both turbocompressors. The centroid radius r_c is predefined as a logarithmic spiral. The tongue or cut-water geometry is not a part of the 1D design. Nonetheless, it is worthwhile to mention that during the detailed

design of the volute, the distance between the tongue and the impeller has been increased (currently tongue placed at approximately $\psi = 30^\circ$) to reduce the pressure distortions from non-uniform flows, as recommended in Dong et al. (1997). Finally, some additional diffusion is obtained in the external diffuser pipe as the volute exit area is increased by approximately 1.5 times the scroll exit area.

Surface roughness and Reynolds number. The surface roughness effect is not included in the 1D calculations, which is a critical parameter for small-scale turbomachinery. The achievable surface roughness and texture depend on the process capability of the manufacturer. Furthermore, the friction coefficient c_f is a function of the Reynolds number $Re = u_2 d_2 / v_{00}$ (definition from Japikse, 1996) and the relative surface roughness k/d_h according to the Moody diagram (Moody, 1944). The Reynolds number is calculated to be approximately 3.3×10^6 and 8.5×10^6 for first and second stage turbocompressors, respectively. Interestingly, despite their small size, the Re is on the higher side compared to geometrically similar air compressors. The influence of relative surface roughness is less dominating as c_f is overall low. This can be one of the main reasons why such small-scale turbocompressors for compressing denser refrigerant fluids can still achieve relatively high isentropic efficiencies in the range of 75–80%, as demonstrated in Schiffmann and Favrat (2009). Nonetheless, further evaluation is required on the influence of surface roughness on refrigerant fluid based miniature turbocompressors.

2.2. 1D turbocompressor performance

Following the extensive design exercise, 1D designs are obtained for the two turbocompressor stages. Table 1 compiles the main compressor geometric and the design point performance data. Considering the geometry, the two turbocompressors will be one of the smallest of their kind with tip diameters d_2 in the order of 15 mm once manufactured and tested. Despite their small size and relatively large tip-clearance (relative tip-clearance $\epsilon = t_{clr}/b_2$ is approximately 13–15%), the compressors are able to achieve isentropic efficiencies in the range of 77% at design point. Off-design performance is equally important for the turbocompressors. Therefore, non-dimensionalized 1D performance maps have been obtained, as shown in Fig. 5. By converting the compressor performance to non-dimensional rotational speed $N_{nd} = Nd_2/a_{00}$ and

Table 1 – Geometric specifications and design point performance calculated by the 1D design tool.

| Geometric data | | |
|---|------------------|------------------|
| Parameter | Compressor no. 1 | Compressor no. 2 |
| Inducer shroud radius, r_{1t} (mm) | 3.62 | 3.43 |
| Tip radius (diameter), r_2 (d_2) (mm) | 7.62 (15.2) | 7.4 (14.8) |
| Tip height, b_2 (mm) | 0.62 | 0.53 |
| Tip-clearance (relative), t_{clr} (ϵ) (mm) | 0.08 (13%) | 0.08 (15%) |
| Blade angle at inducer tip, β_{1b} (deg) | 57° | 57° |
| Backsweep angle, β_{2b} (deg) | 45° | 45° |
| Diffuser radius, r_5 (mm) | 12.57 | 12.22 |
| Diffuser height, b_5 (mm) | 0.405 | 0.42 |
| Volute outlet diameter, d_7 (mm) | 5.37 | 4.74 |

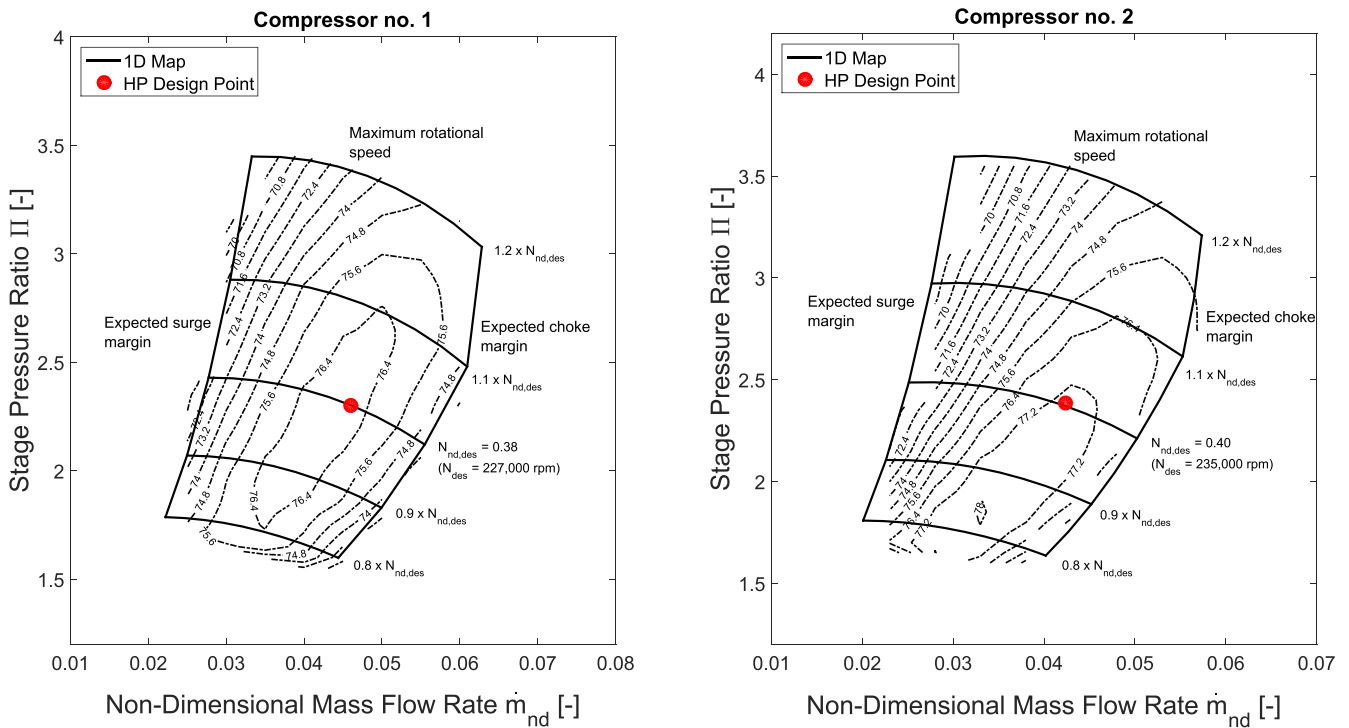


Fig. 5 – 1D compressor maps for first and second stage turbocompressors with isentropic efficiency contours.

non-dimensional mass flow rate $\dot{m}_{nd} = \dot{m}/(\rho_{00}a_{00}d_2^2)$, the influence of varying inlet conditions with a real gas is removed (Dixon, 2005). Empirical stall checks provided in the 1D design tool for different stage components have been monitored at low mass flow rate operations. Although higher level of modeling and experimentation is required to obtain the actual operating range, some performance indicators can be evaluated, as shown in Fig. 6, to foresee compressor off-design instabilities.

Operating range. Considering the stable operating range $R = \frac{\dot{m}_{choke} - \dot{m}_{surge}}{\dot{m}_{choke}}$ at design rotational speed, the two turbocompressors are in a relatively high range category with R reaching 50% for moderately low flow coefficient compressors having a design pressure ratio around 2.3–2.5 according to Japikse (1996). Note that in Fig. 5, the choke line represents mass flow rates approximately 10–15% lower than the calculated choke mass flow rates. This margin has been provided to accommodate any additional blade blockage due to the presence of hub fillets and deviations in blade thickness after manufacturing.

Inducer performance. Focusing on the inducer performance in Fig. 6(a), the incidence angle at inducer tip i_{1t} varies from approximately -5° to 14° from maximum to minimum mass flow rate in the 1D compressor map. At the lowest mass flow rate operation, the relative tip Mach number $M_{1t,rel}$ is in the range of 0.6 (benefit of lower inducer hub diameter). For common industrial stages, critical i_{1t} is about 18° to 20° at $M_{1t,rel} = 0.6$ beyond which an inducer stall is likely to occur according to a survey given in Japikse (1996). Therefore, a stable inducer performance is expected for both turbocompressors.

Exducer performance. The exducer performance given in Fig. 6(b) is evaluated by the amount of diffusion in the impel-

ler passage. The diffusion ratio DR reaches approximately 1.9 at the lowest mass flow rate operation for both turbocompressors. This is still lower than the critical DR=2.0 set by the minimum De-Haller criterion of 0.5. Also the impeller exit swirl $\lambda_{2m} = 8$ is reached at the lowest mass flow rate, which corresponds to $\alpha_{2m} = 82^\circ$ approximately.

Vaneless diffuser performance. Considering the vaneless diffuser performance in Fig. 6(c), the critical flow angle α_c is estimated in the range of 80° to 82° (equivalent to λ_5 of around 6.0 to 8.0). The estimation is based on b_2/r_2 and α_c correlated data provided in Jansen (1964), Japikse (1996) and Senoo and Kinoshita (1977), and the 1D model. Due to pinching from approximately $b_2/r_2 = 0.07$ – 0.08 to a new ratio $b_3/r_2 = 0.053$ – 0.056 , the critical flow angle α_c is increased from 75° to 82° , thereby increasing diffuser stability at low mass flow rate operation for the two turbocompressors. The diffuser pressure recovery coefficient $C_{p,vld} = \frac{p_5 - p_{2m}}{p_{02m} - p_{2m}}$ in the first stage compressor is somewhat lower than the second stage with slightly higher pressure loss $K_{vld} = \frac{p_{02m} - p_{05}}{p_{02m} - p_{2m}}$ due to a larger pinch.

Volute performance. Considering the volute performance in Fig. 6(d), at the design point, no pressure recovery takes place in the scroll part (where the volute pressure recovery coefficient is $C_{p,vol} = \frac{p_6 - p_5}{p_{05} - p_5}$). Nonetheless, there is a pressure recovery taking place in the diffuser pipe (not plotted here). Minimum loss coefficient $K_{vol} = \frac{p_{05} - p_{06}}{p_{05} - p_5}$ is obtained at around the design diffuser exit swirl parameter λ_5 . The second stage turbocompressor volute exhibits lesser loss due to higher λ_5 (lesser loss from the meridional velocity component c_{m5} en-

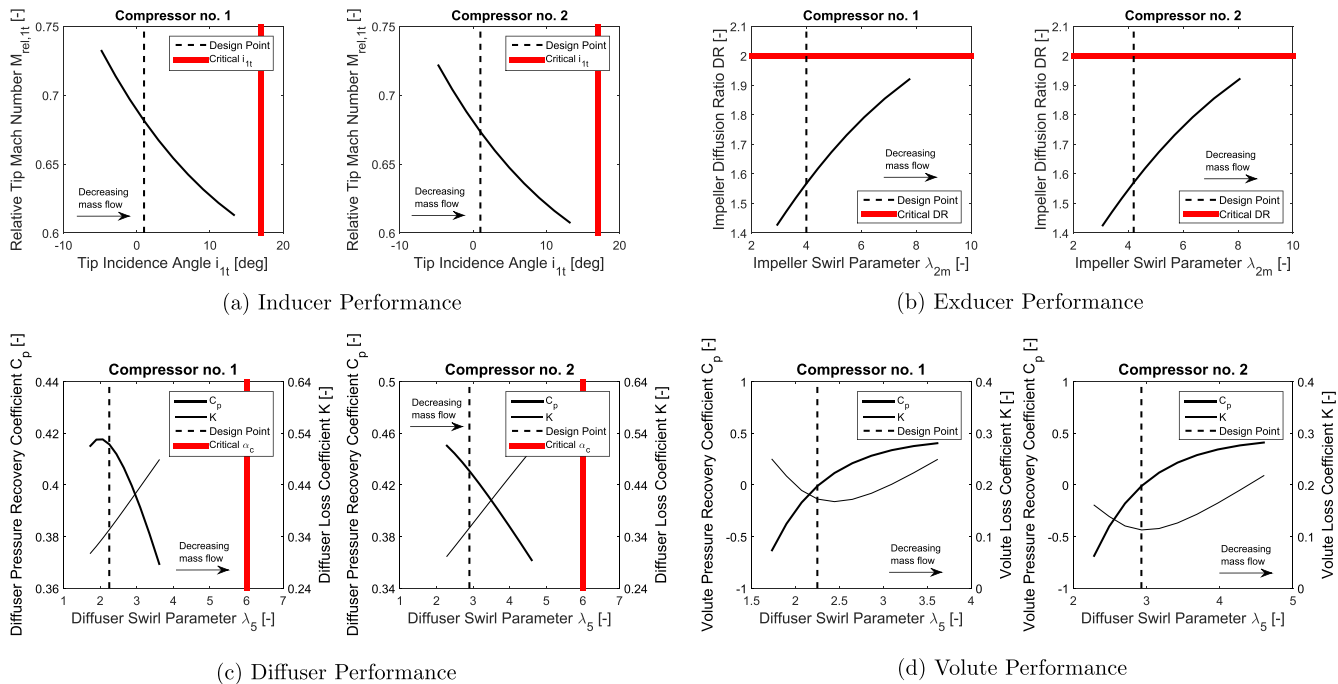


Fig. 6 – Critical evaluation of different compressor components at their respective design speed lines.

tering the volute). At lower mass flow rate operation, the scroll also diffuses the flow and could eventually enter a stall mode. However, strong swirling flow in the volute should delay the stall (Japikse, 1981). The components upstream could be influenced considerably by the pressure rise and accompanying distortions though. The volute stall limit is presently unknown and is intended to be studied during experimentation.

3. Stochastic evaluation of off-design heat pump performance

The 1D compressor performance maps for the two turbocompressor stages are primarily used to obtain estimates of isentropic efficiencies at heat pump off-design operating conditions. The extent of stable heat pump and turbocompressor operation and the heat pump performance in form of COP variation has also been evaluated.

3.1. Data interpolation from 1D compressor performance maps

A conventional piece-wise linear interpolation scheme based on Munzberg and Kurzke (1977) has been applied for off-design simulation of a two-stage refrigeration cycle operating with turbocompressors in Turunen-Saaresti et al. (2010). A direct COP evaluation is, therefore, obtained in relation to compressor performances, but within their specific operating ranges. For estimating combined heat pump and turbocompressor performances in the present application, the triangulation-based scattered interpolation function provided in Matlab has been used instead. The method is efficient and particularly ad-

vantageous due to its extrapolation functionality (Amidror, 2002).

3.2. Monte Carlo simulation with the heat pump model

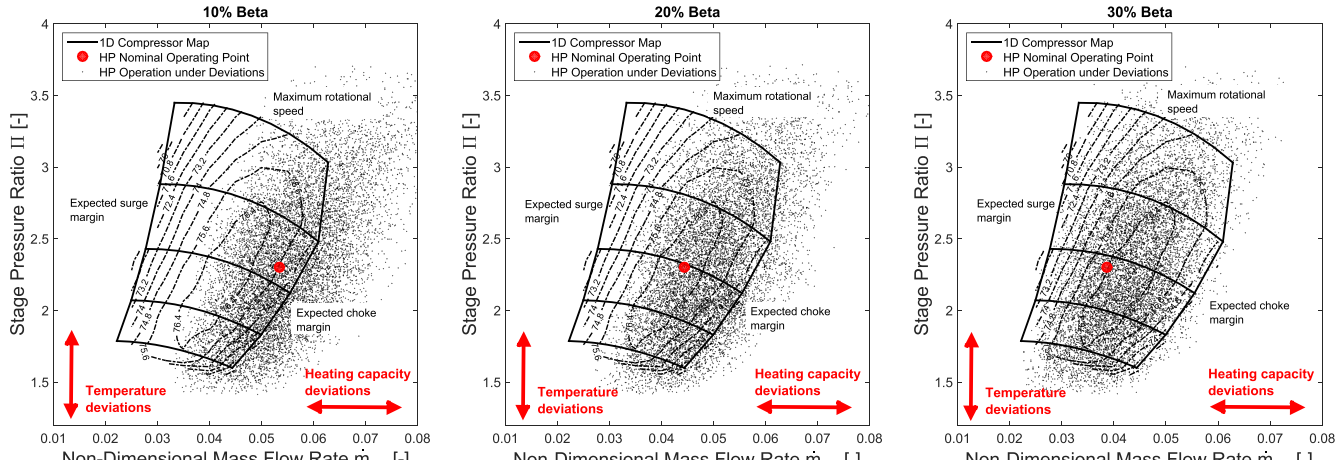
Monte Carlo method applies stochastic sampling to compute the complete statistics of the response quantities of interest with an arbitrary level of accuracy provided sufficient number of samples is used (Keane and Nair, 2005). A total of 10,000 Monte Carlo samples of uniformly distributed random input parameter variations have been simulated with the heat pump model. The heat pump input parameters and their respective deviations are summarized in Table 2. Uniform probability distribution is the simplest of distributions in which all the quantities of a random input variable occur with equal probability. The computed results can, therefore, be considered as conservative estimates of the actual predictions in the absence of measured input variability data.

3.3. Off-design turbocompressor performance under deviations

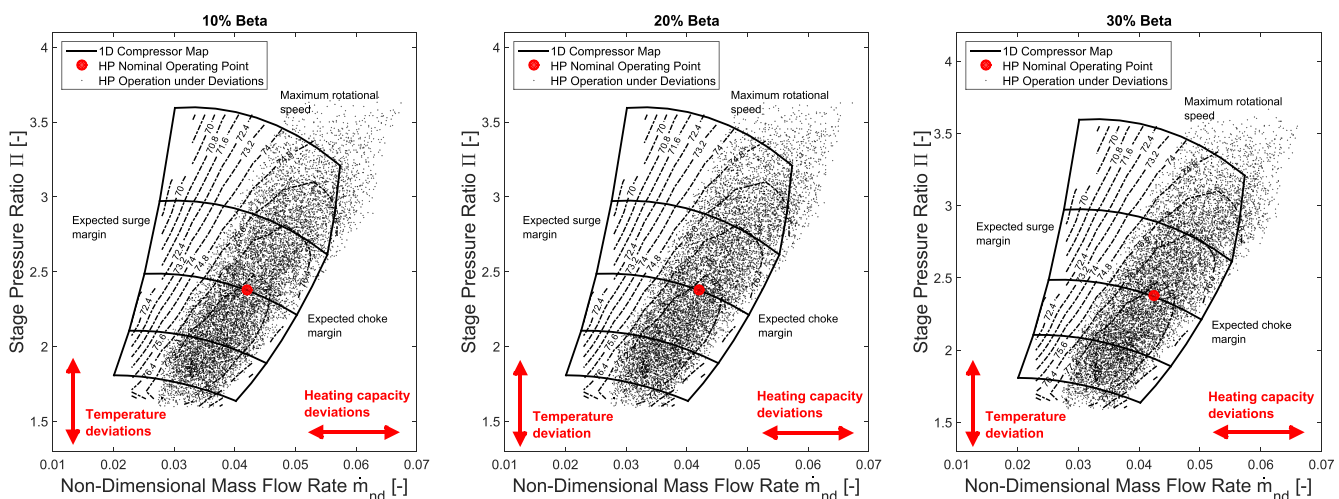
Two assumptions have been made during the stochastic evaluation: (1) the temperature drops across source and sink fluid

Table 2 – Heat pump operating parameters and their deviations.

| Parameter | Nominal | Deviation |
|---|----------------|-----------|
| 1st source temperature, T_{evap} [°C] | 5 | ±5 |
| 2nd source temperature, T_{int} [°C] | 30 | ±10 |
| Sink temperature, T_{cond} [°C] | 55 | ±5 |
| Condenser heating capacity, \dot{Q}_{cond} [kW] | 6.5 | ±1 |
| 2nd source heat capacity, \dot{Q}_{int} [kW] | 10–30% β | ±0.5 |



(a) First stage turbocompressor – Compressor no. 1



(b) Second stage turbocompressor – Compressor no. 2

Fig. 7 – Off-design turbocompressor operation with stochastic variation in heat pump operating conditions and the influence of the second source heat increase from 10 to 30% β .

streams are kept constant by adjusting their respective mass flow rates for more stable regulation of pressures in the heat exchangers, and (2) the turbocompressors are able to operate beyond their expected operating ranges (data are thus extrapolated) since the actual operating ranges are not known at this point. These aspects will be studied in more detail during the experimental phase.

Fig. 7 shows the influence of random heat pump parameter deviations on the two turbocompressor stages for 10–30% β second heat source addition. The temperature and heat capacity deviations cause a variation in compressor pressure ratios and mass flow rates, respectively. Each point on the compressor maps represents a possible operating point as a result of the heat pump operational deviations. The location of the operating point within the compressor map has a direct effect on the compressor efficiency and thus on the heat pump performance.

Focusing on the first stage turbocompressor plots in Fig. 7a, a large performance variation is observed as it accommo-

dates the random deviations (both temperature and heat capacity) from the second heat source as well in addition to the random deviations from the condenser. For the 20% β case (included in the compressor design point specifications), most of the off-design operating points are within the expected operating range. However, some operating points are exceeding the maximum rotational speed and choke limits. As the second heat source capacity is reduced to 10% β , the operating points shift more toward higher mass flow rates, thus exceeding the choke margin considerably to provide the required condenser heat. On the contrary, for 30% β second source heat, the operating points move toward the surge margin. Interestingly, the compressor operating range is wide enough to accommodate almost all the heat pump off-design operation except those exceeding the maximum rotational speed limit.

The second stage turbocompressor operates within a smaller spread of off-design heat pump operating points as shown in Fig. 7b. The second heat source does not influence the mass

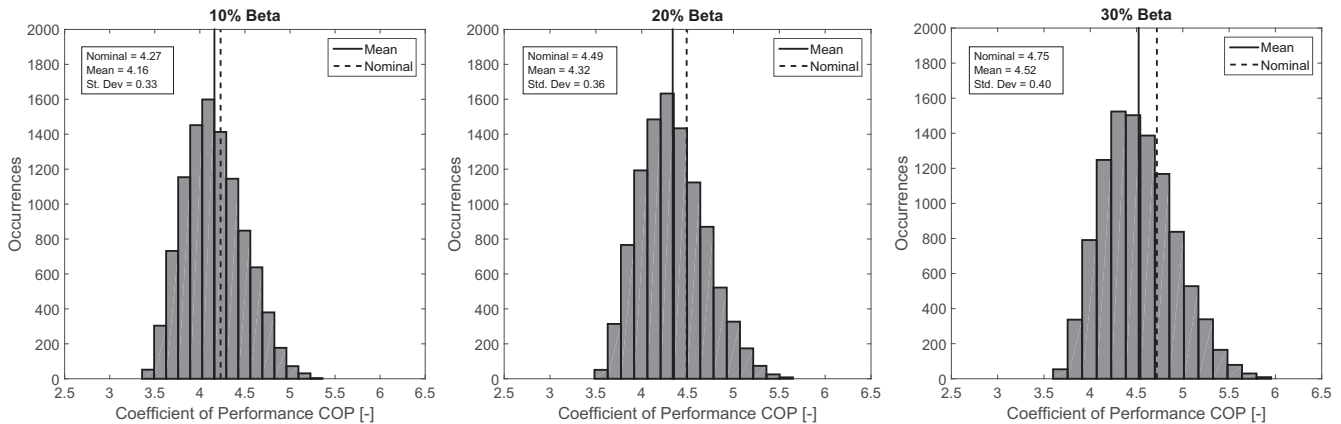


Fig. 8 – Heat pump performance under deviations in operating conditions.

flow rate variations in this case and effect of condenser heat capacity deviations is only seen. Nonetheless, the maximum rotational speed and choke limits are being exceeded in few off-design operating points.

3.4. Off-design heat pump performance under deviations

The off-design performance of the two-stage heat pump is statistically summarized as COP probability distributions in Fig. 8 for different β levels. The nominal COP increases by 10% from 4.27 to 4.75, while the mean COP increases by 8% from 4.16 to 4.52 with 10–30% β second source heat addition. Furthermore, the COP standard deviation increases from 0.33 to 0.40. Note that the mean COP levels are actually lower than the nominal COP levels, thereby indicating a systematic heat pump performance shift under stochastic input parameter deviations. This systematic shift also increases in magnitude with increase in β levels.

4. 3D turbocompressor impeller design

The passage flow in centrifugal compressors is non-uniform and divided into a distinct (nearly) isentropic primary flow zone and a low-momentum non-isentropic secondary zone. As the flow leaves the impeller blades, the two zones undergo a rapid mixing causing a significant performance loss. An appropriate 3D impeller blade design suppressing the secondary zone is, therefore, very important. Modern turbomachinery design methods utilize complex black-box optimization algorithms supplemented with fast metamodels (Bonaiuti et al., 2006; Kim et al., 2010, 2011; Verstraete et al., 2010). However, such approach also requires a considerable effort to build the appropriate metamodels that can incorporate a suitable number of design variables. On the contrary, a more theoretical and observation based approach has been applied to design the turbocompressor impellers using steady-state CFD with Ansys CFX. Note that the first stage turbocompressor impeller has been optimized. Similar blading is to be applied for the second stage turbocompressor impeller.

4.1. CFD setup

The following steps have been taken to set up an appropriate CFD model of the turbocompressor stage:

3D geometric model. The 1D geometric data have been used to construct a 3D geometric model using ANSYS BladeGen. The model consists of a straight inlet duct, impeller and the vaneless diffuser in a single passage fluid domain as illustrated in Fig. 9. The impeller meridional hub and shroud profiles have been defined by Bézier curves of 5th order (six control points). The blade shape is controlled by the wrap angle θ at the hub and shroud profiles also defined by 5th order Bézier curves. Maximum wrap angle $\theta = 70^\circ$ has been defined at the impeller TE hub and shroud to keep the blade length and curvature in control, while having a zero blade lean. The LE has an elliptic ratio of 2.0 and the TE is cut-off. The blade thickness is consistent in the span-wise (hub-to-shroud) and stream-wise directions (LE to TE). The hub fillets are not included. The splitter blades begin from a meridional distance of approximately 40% from the LE and follow the blade angle and

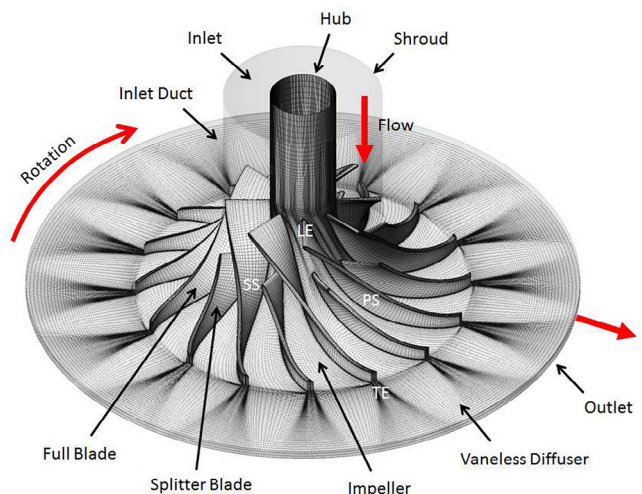


Fig. 9 – Illustration of the full computational domain and grid.

Table 3 – Grid independence study.

| Parameter | 0.28 million | ← %Δ → | 1.2 million | ← %Δ → | 4.0 million |
|-------------------------------|--------------|--------|-------------|--------|-------------|
| Pressure ratio, Π | 2.41 | 3.15% | 2.49 | 0.76% | 2.51 |
| Isentropic efficiency, η | 78.0% | 1.9% | 79.5% | 0.63% | 80.0% |

thickness distributions of the full blades till the TE. Note that the volute is not included in the present CFD study to reduce the computational cost during impeller blading design.

Grid processing. A 3D structured grid has been created using the H-Grid and O-Grid topologies in ANSYS TurboGrid. The near-wall y^+ has been maintained approximately equal to 1 to resolve the viscous sublayer in the turbulent boundary layer except the TE of the impeller blades, where a fine near-wall grid could not be constructed. The tip-clearance gap is also introduced in the grid processing tool by trimming down the impeller shroud profile. A grid independence study has been made by simulating three different grid sizes containing 0.28 million, 1.2 million and 4.0 million hexahedral elements at design point. The overall pressure ratio and isentropic efficiencies (inlet to diffuser outlet) have been compared in Table 3. As evident, the difference %Δ between the compressor properties reduces with increase in grid size. Based on the grid independence study, grid size of 1.2 million elements is a suitable choice.

Solver setup. Fig. 9 also illustrates the different boundary conditions applied to the compressor fluid domain. Since a single passage simulation is considered, the symmetric surfaces are defined as periodic boundaries. The interfaces between the inlet duct, impeller and the vaneless diffuser are defined as stage/mixing plane. The impeller shroud is set as counter-rotating wall to model the relative motion between the rotating impeller and a stationary shroud. All the wetted surfaces have been considered as hydraulically smooth; hence surface roughness is not defined and skin friction loss is only caused by fluid viscosity. The total inlet conditions have been defined at the inlet boundary, while design mass flow rate is defined at the outlet boundary of the domain. Refrigerant fluid R134a has been set as the fluid medium. The $k-\omega$ shear stress transport (SST) turbulence model (Menter, 1993) has been specified for all the CFD analyses. A moderate turbulence intensity of 5% has also been maintained at the inlet boundary.

4.2. Blade passage design

The flow field has been studied and relevant measures are taken to control and limit the secondary flow production in the impeller passages as follows:

Secondary flow and tip-leakage. Many important analytical and experimental studies have been made to quantify the flow field in centrifugal compressors (Casey et al., 1992; Eckardt, 1975, 1976; Hirsch et al., 1996; Johnson, 1978; Krain, 1981). According to these studies, the flow field in a centrifugal compressor stage is highly complex and subjected to local accelerations due to centrifugal forces (curvature effect) and Coriolis forces (rotational effect). The resulting pressure gradients generate secondary flow in shape of streamline vorticity along the end-walls (hub and shroud surfaces) from pressure side (PS) to the suction side (SS) due to blade-to-blade curvature, secondary flow along the blade surfaces (span-wise direction) due to me-

ridional curvature, and the secondary flow generated by the Coriolis forces mainly in the radial parts of the impeller. The tip-leakage flow due to the migration of high pressure flow from PS to SS of the blades through the tip-clearance gap supplements the secondary zone by forming a large vortex that stretches stream-wise in the blade passages causing a considerable performance loss. With 10% increase in the relative tip-clearance, large efficiency drops in the range of 3–6% have been reported in Backman et al. (2007), Klassen et al. (1977), Olivero et al. (2011) and Pampreen (1973). Interestingly, more performance penalty is observed in backswept impellers compared to radial impellers (Ishida et al., 1990).

Optimum blade loading distribution. Principally, the blade-to-blade loading coefficient $\Lambda = \frac{w_{ss} - w_{ps}}{\bar{w}}$ (where $\bar{w} = \frac{w_{ss} + w_{ps}}{2}$) is used to express the distribution of work along the blade passage. The suppression of secondary flow and subsequent performance improvement in centrifugal compressors has been attempted by applying the inverse design method (Shibata et al., 2011; Zangeneh et al., 1998, 2011). A loading distribution is specified and the blade angles are defined accordingly along the passage length. Classically, a more mid- and aft-loaded blading with moderate loading in the inducer has been suggested for centrifugal compressors (Dallenbach, 1961; Japikse and Osborne, 1986). A fore-loaded distribution at the shroud and aft-loaded distribution at the hub is suggested instead in Zangeneh et al. (1998) for suppressing the secondary flow. Finally, a more arbitrary and front-loaded blading distribution has been applied for improved efficiency and operating range in Yagi et al. (2008). A consensus is hence not found in the literature.

Interestingly, the inverse design method does not consider the all-important tip-leakage flow. The blade loading distribution has a direct influence on the static pressure properties over the blades. Reduced sensitivity to tip-clearance can be achieved through moderate blade loading (Palmer and Waterman, 1995). Moreover, the test cases presented in such studies comprise of large-scale centrifugal compressors, which are usually not constrained by manufacturing and assembly limits and can accommodate a large number of blades (thus lower loading per blade) with small relative tip-clearances ($\varepsilon < 5\%$). For small-scale turbomachinery, such as the turbocompressors designed in this study, the tip-leakage flow due to large relative tip-clearance ($\varepsilon \approx 15\%$) will dominate the overall flow field in the blade passages. In this case, a fore-loaded shroud, as suggested in Zangeneh et al. (1998), can cause a large tip-leakage vortex initiating at the LE and occupying a larger passage area. Furthermore, a fore-loaded shroud can also result in lesser choke margin and a higher shock loss (more related to high flow coefficient and transonic compressors). Hence, a suitable blade loading distribution has to be defined taking into account the influence of large tip-clearance gap and the associated leakage for the turbocompressors.

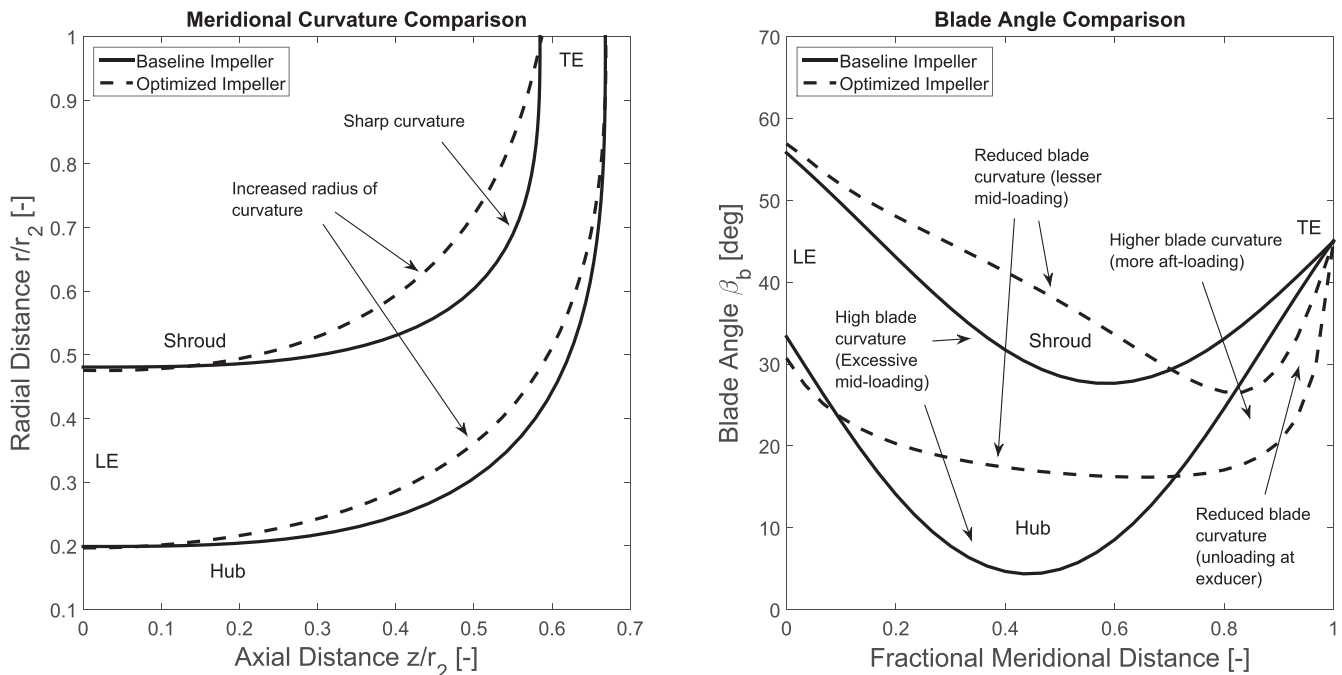


Fig. 10 – Comparison between the baseline and the optimized impeller blade designs.

Baseline impeller geometry and flow field. Fig. 10 shows the comparison between the baseline and optimized impeller designs. Focusing on the baseline design (basic design produced by ANSYS BladeGen with 1D geometric data), evidently the shroud radius of curvature is small in the axial-to-radial bend, which can have a large contribution to the secondary flow production because of a hub-to-shroud or span-wise velocity imbalance (Johnson, 1978). The blade curvature is also large (smaller blade angles) between 30 and 60% of the passage length followed by a large reduction till the TE. Fig. 11 shows the relative velocity and entropy contours for the baseline design. From the inducer shroud, the flow rapidly decelerates till the axial-to-radial bend, where it accelerates considerably till the TE. The

sharp curvature and also to some extent, a narrow passage area, advance the acceleration. The tip-leakage flow is also located in the shroud region, but is overshadowed by the accelerated flow. A highly non-uniform flow pattern is, therefore, seen at the TE of the impeller. Near to the shroud, large entropy production is seen at the TE on the pressure side of the blades in addition to the tip-leakage loss. Fig. 12 provides the near-shroud relative velocity distribution and blade loading coefficient along the full blade passage. The above mentioned deceleration is seen between 20 and 30% of the blade passage causing a sudden dip in blade loading. The blades are highly loaded with $\Lambda > 1$ between 30 and 60% of the passage length where the blade curvature is maximum. This is

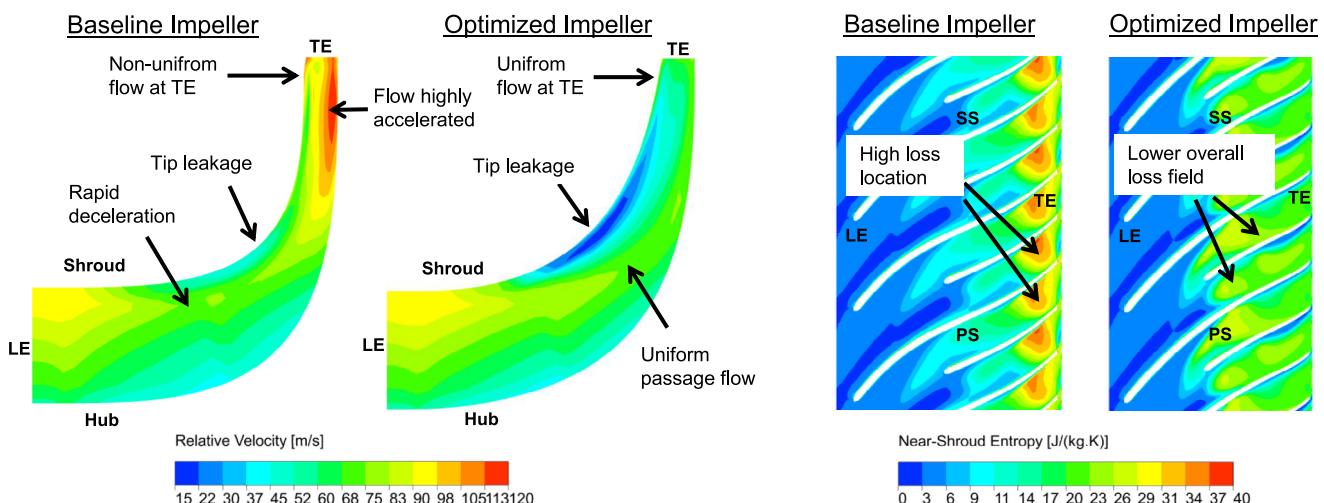


Fig. 11 – Comparison between the baseline and the optimized impeller flow fields as relative velocity contours (left) and near-shroud (85% blade span) blade-to-blade entropy field (right).

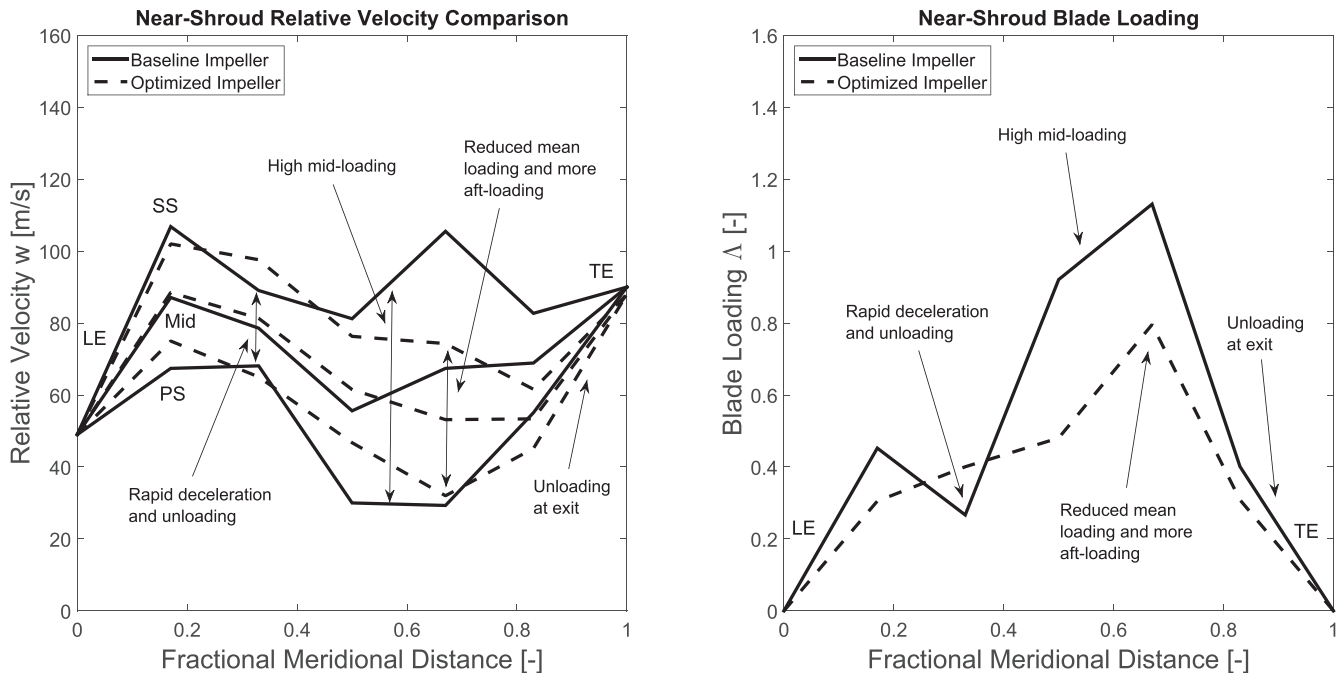


Fig. 12 – Near-shroud (85% blade span) loading comparison between baseline and optimized impeller designs as relative velocity distribution (left) and blade loading coefficient (right) along the full blade.

followed by a rapid unloading causing the accelerated and non-uniform flow field at the TE of the impeller.

Methodology for optimized design. Although each impeller design is a new problem, a good blade passage can be designed by controlling the meridional and blade-to-blade curvatures in order to have a uniform velocity or pressure distribution in the blade passages, thus reducing the secondary and tip-leakage flows. Hence, the following steps have been taken to iteratively optimize the impeller design:

- The baseline impeller design has been carefully studied to identify critical locations where the flow is accelerated and how the blade loading influences the tip-leakage flow in the blade passages.
- The excessive meridional curvature has been reduced at the hub and shroud to have a more circular axial-to-radial bend. The small hub diameter facilitates the design of a smooth circular channel.
- The mean blade loading has been reduced in the middle section of the impeller passages by reducing the blade curvature (approximately 10° higher mean blade angle compared to the baseline impeller). Furthermore, the blade curvature is maximum between 60% and 80% of the passage length, which ensures an aft-loaded blading.
- The influence of Coriolis force (dominant in the radial part of the impeller) has been reduced by lowering the blade curvature from 80% of the passage length till the TE of the impeller. This arrangement unloads the exducer section.
- The presence of splitter blades further helps in reducing the average loading per blade and reduce the tip-leakage flow.

Baseline and optimized impeller flow field comparison. Following the design optimization, the impeller achieves a more

balanced flow field as seen by the relative velocity contours in the meridional channel in Fig. 11. The flow continually decelerates from the inducer ending up in a uniform flow field at the TE. The tip-leakage flow is concentrated in the axial-to-radial bend near to the shroud, while overall entropy is also reduced. Typically the blade loading coefficient is limited approximately in the range of 0.7 and 1.0 (Japikse, 1996). In Fig. 12, maximum blade loading is observed between 60% and 80% of the passage length (thus aft-loaded blading) with $\Lambda < 0.8$ peak value, which is acceptable.

Tip-leakage flow comparison. Fig. 13 presents a detailed picture of the tip-leakage flow for the baseline and optimized impeller designs. Looking at the baseline impeller flow field, the blade passages are engulfed with large amount of vorticity originating mainly from the tip-leakage flow. A large tip-leakage vortex initiates from the LE shroud, which moves towards the splitter blade SS and stretches to the TE forming a large loss region indicated by the TE entropy contours. Due to high mid-loading, an excessive tip-leakage also appears and swirls in the mid-passage region. Fig. 13 also shows the end-wall and blade surface secondary flows. As expected, the secondary flow moves from the PS to SS across the hub surface (blade-to-blade) and span-wise from hub to shroud. In comparison, the optimized impeller shows an improved vorticity structure in the blade passages. Similar to the baseline impeller, the tip-leakage initiates at the LE shroud and propagates to the splitter blade SS mixing with the tip-leakage flow originating from the splitter blade. Unlike the baseline impeller, this tip-leakage vortex is more aligned with the SS of the splitter blades. Some more leakage flow is seen in the aft-sections of the blade passages. Overall, the flow field contains lesser vorticity, which results in a more uniform flow and lesser entropy production at the TE compared to the baseline impeller. The end-wall and blade

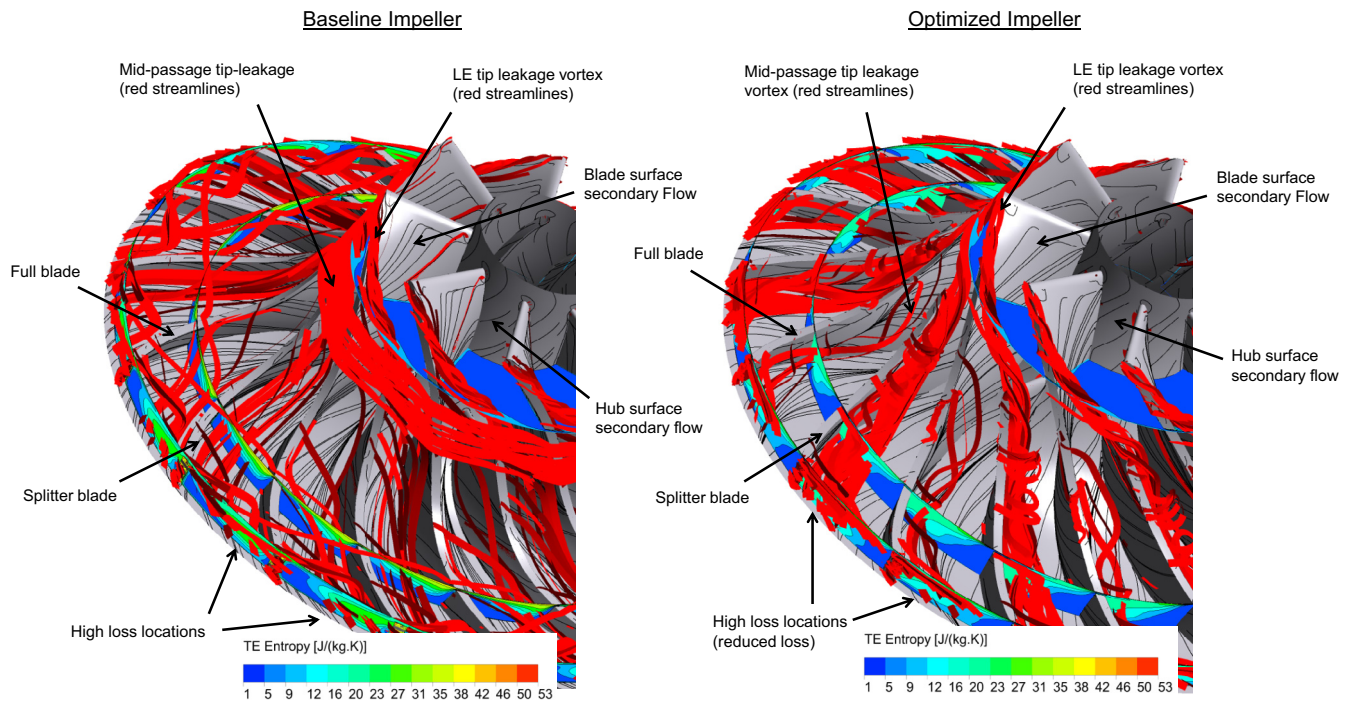


Fig. 13 – Comparison of secondary and tip-leakage flow between the baseline and optimized impeller designs.

surface secondary flows appear to be improved slightly. However, it is extremely challenging to control the secondary flow in the presence of large tip-leakage flow.

Overall performance comparison. Fig. 14 shows a performance comparison between the 1D design, and 3D CFD based baseline and optimized compressor designs at the design speed line. Note that these performance numbers are based on the CFD domain comprising of the inlet duct, impeller and the

vaneless diffuser only. With an improvement in the flow field, the design point performance also increased significantly for the optimized impeller compared to the baseline. The pressure ratio increased by approximately 15% from 2.13 to 2.48, while isentropic efficiency increased by 3.5% points from 76% to 79.5%. The baseline design performs poorly in general, as seen by severe performance loss along the speed line. The optimized compressor also gives better performance compared

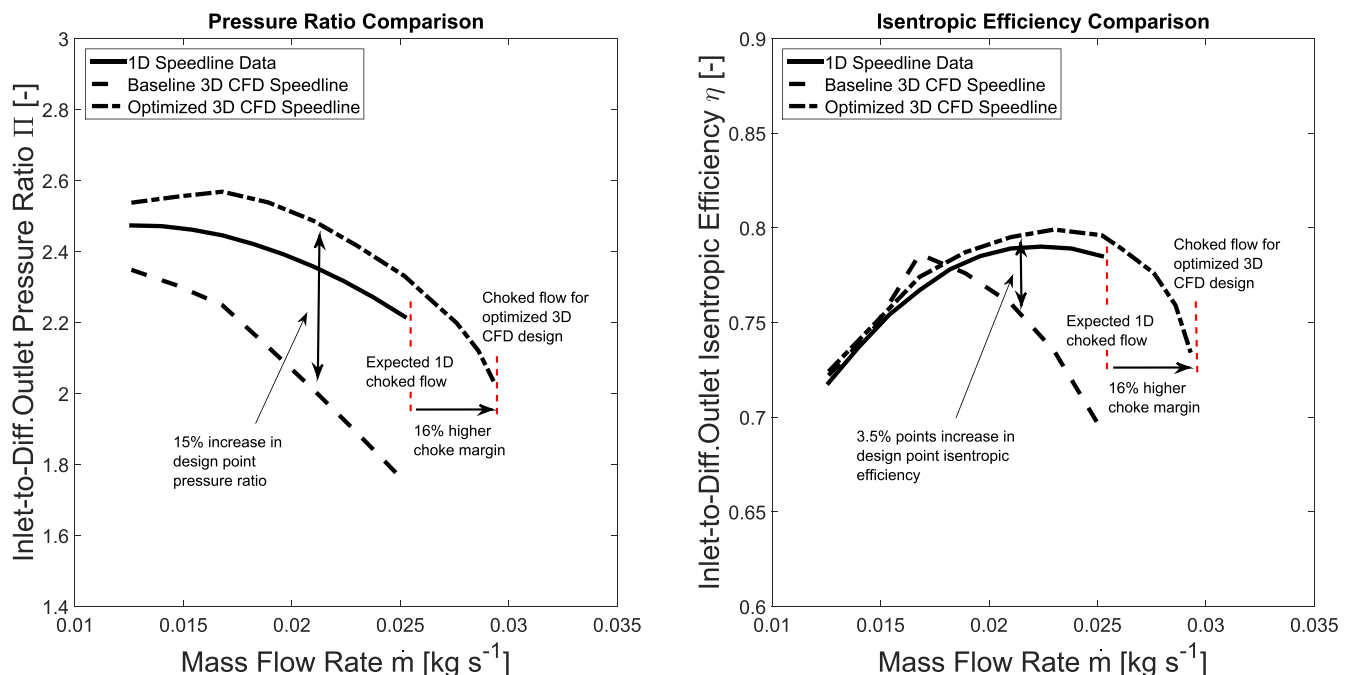


Fig. 14 – Compressor inlet to diffuser outlet performance comparison at the design speed line.

to the 1D model, which validates the proposed approach. To estimate the choke mass flow, static pressure has been defined at the domain outlet boundary and gradually reduced till mass flow rate does not increase any further. Approximately 16% higher choke mass flow rate than the 1D model prediction is expected from the optimized compressor design, thus increasing the compressor operating range R to almost 57% at design rotational speed.

5. Conclusions

A detailed methodology has been presented in this paper on the design of miniature turbocompressors for wide-range operation in the presence of large tip-leakage flow. The following conclusions can be drawn from this study:

- The stochastic performance evaluation exposes the difference between nominal heat pump performance and the performance under deviating operating conditions. An integrated heat pump and 1D design optimization could be studied, where the system is robustly designed for maximizing the compressor operating range and heat pump performance in general.
- Smaller hub diameters improve the impeller and overall compressor performance by allowing a lower relative velocity at the inducer tip. The blade design can also benefit from a more circular channel and improved flow at the TE of the impeller. However, it is not always possible to have a low hub diameter due to shaft diameter and blading constraints, especially for extremely small-scale compressors.
- For a wide operating range, a careful balance between the work transfer in the impeller and vaneless diffuser performance is necessary. A pinched vaneless diffuser can improve the work transfer in the impeller, while allowing the diffuser to operate stably at off-design conditions.
- For small-scale compressors, the large relative tip-clearance ($\epsilon > 5\%$) and the associated tip-leakage flow dominate the overall flow field in the impeller passages. A moderate overall blade loading and more aft-loaded distribution is found to be most favorable blading in the present case. The overall flow structure and compressor performance have increased substantially by following the design methodology described in the paper.
- Miniature inlet guide vanes and low-solidity vaned diffusers could be studied in a future project to enhance the operating range and peak efficiency of the first stage turbocompressor.

Acknowledgments

The authors would like to thank the Swiss Competence Center for Energy Research on Efficiency of Industrial Processes (SCCER EIP) and the Swiss Federal Office for Energy (SFOE) (Project no. SI/501185) for their financial support, and Prof. Michael Casey and Dr. Daniel Rusch for their useful discussions and insights.

REFERENCES

- Amidror, I., 2002. Scattered data interpolation methods for electronic imaging systems: a survey. *J. Electron. Imaging* 11 (2), 157–176.
- Arpagaus, C., Bless, F., Schiffmann, J., Bertsch, S., 2016. Multi-temperature heat pumps a literature review. In: Proceedings of International Refrigeration and Air Conditioning Conference. Purdue University, West Lafayette, IN, pp. 1–10. Paper ID 2021.
- Aungier, R., 2000. Centrifugal Compressors – A Strategy for Aerodynamic Design and Analysis. American Society of Mechanical Engineers (ASME) Press, New York.
- Backman, J., Reunannen, A., Saari, J., Turunen-Saaresti, T., Sallinen, P., Esa, H., 2007. Effects of impeller tip-clearance on centrifugal compressor efficiency. In: Proceedings of ASME Turbo Expo. Montreal, Canada. 86-GT-221.
- Baines, N., 2005. Fundamentals of Turbocharging. Concepts ETI, Hartford, VT.
- Balje, O., 1981. Turbomachines, a Guide to Design, Selection and Theory. John Wiley & Sons, New York.
- Bertsch, S., Groll, E., 2008. Two-stage air-source heat pump for residential heating and cooling applications in northern U.S. climates. *Int. J. Refrigeration* 31, 1282–1292. doi:10.1016/j.ijrefrig.2008.01.006.
- Bonaiuti, D., Arnone, A., Ermini, M., Baldassarre, L., 2006. Analysis and optimization of transonic centrifugal compressor impellers using the design of experiment technique. *ASME J. Turbomach.* 128, 786–797.
- Casey, M., 2012. Vorlesungsmanuskript zu turbokompressoren und ventilatoren. Course Note; ITSM Universität Stuttgart.
- Casey, M., Dalbert, P., Roth, P., 1992. The use of 3D viscous flow calculations in the design and analysis of industrial centrifugal compressors. *ASME J. Turbomach.* 114, 27–37.
- Chua, K., Chou, S., Yang, W., 2010. Advances in heat pump systems: a review. *J. Appl. Energ.* 87, 3611–3624. doi:10.1016/j.apenergy.2010.06.014.
- Cumpsty, N., 2004. Compressor Aerodynamics. Krieger Publishing Company, Malabar, FL.
- Dallenbach, F., 1961. The aerodynamic design and performance of centrifugal and mixed-flow compressors. In: SAE Technical Paper Series. 610160.
- Dean, R., 1974. The Fluid Dynamic Design of Advanced Centrifugal Compressors. Lecture Series. Von Karman Institute for Fluid Dynamics (VKI), Hanover, NH.
- Demierre, J., Favrat, D., Schiffmann, J., Wegele, J., 2014. Experimental investigation of a thermally driven heat pump based on a double organic cycle and an oil-free compressor-turbine unit. *Int. J. Refrigeration* 44, 91–100. doi:10.1016/j.ijrefrig.2014.04.024.
- Dixon, S., 2005. Fluid Mechanics, Thermodynamics of Turbomachinery. Elsevier Inc., Oxford, UK.
- Dong, R., Chu, S., Katz, J., 1997. Effect of modification to tongue and impeller geometry on unsteady flow, pressure fluctuations, and noise in a centrifugal pump. *ASME J. Turbomach.* 119, 506–515.
- Eckardt, D., 1975. Measurements in the jet-wake discharge flow of a centrifugal compressor impeller. *ASME J. Eng. Power* 97 (3), 337–346.
- Eckardt, D., 1976. Detailed flow investigations within a high speed centrifugal compressor impeller. *J. Fluids Eng.* 98, 390–402.
- Favrat, D., Nidegger, D., Reymond, D., Courtin, G., 1997. Comparison between a single-stage and a two-stage air to water domestic heat pump with on variable speed compressor. In: Proceedings of the IIR Conference on Heat Pump Systems, Energy Efficiency and Global Warming. Linz, Austria.

- Favrat, D., Marechal, F., Epelly, O., 2008. The challenge of introducing an exergy indicator in a local law on energy. *J. Energ.* 33, 130–136. doi:10.1016/j.energy.2007.10.012.
- Granwehr, E., Bertsch, S. Heat pump. Patent WO 2012/040864 A1; 2012.
- Hildebrandt, A., Genrup, A., 2007. Numerical investigation of the effect of different back sweep angle and exducer width on the impeller outlet flow pattern of a centrifugal compressor with vaneless diffuser. *ASME J. Turbomach.* 129, 421–433. doi:10.1115/1.2447873.
- Hirsch, C., Kang, S., Pointel, G., 1996. A numerically supported investigation of the 3D flow in centrifugal impellers – part II: secondary flow structure. In: Proceedings of ASME International Gas Turbine and Aeroengine Congress and Exhibition. Birmingham, UK. 96-GT-152.
- Ishida, M., Senoo, Y., Ueki, H., 1990. Secondary flow due to tip clearance at the exit of centrifugal impellers. *ASME J. Turbomach.* 112, 19–24.
- Jansen, W., 1964. Rotating stall in a radial vaneless diffuser. *ASME J. Basic Eng.* 119, 750–758.
- Japikse, D., 1981. Stall, stage stall and surge. In: Proceedings of 10th Turbomachinery Symposium. Texas A&M Engineering Experiment Station – Turbomachinery Laboratory, Texas, USA.
- Japikse, D., 1984. A critical evaluation of stall concepts for centrifugal compressors and pumps – studies in component performance part 7. In: Proceedings of ASME Winter Annual Meeting. American Society of Mechanical Engineers (ASME), New Orleans, USA.
- Japikse, D., 1985. Assessment of single- and two-zone modeling of centrifugal compressors. studies in component performance: part 3. In: Proceedings of Gas Turbine Conference and Exhibit. Houston, Texas.
- Japikse, D., 1996. Centrifugal Compressor Design and Performance. Concepts ETI, Hartford, VT.
- Japikse, D., Osborne, C., 1986. Optimization of industrial centrifugal compressors – eight design cases from 1972 to 1982. In: Proceedings of Gas Turbine Conference and Exhibit. 86-GT-221.
- Javed, A., 2014. Robust Design of a Micro Centrifugal Compressor. Delft University of Technology, Netherlands.
- Javed, A., Olivero, M., Pecnik, R., van Buijtenen, J., 2011. Performance analysis of a microturbine centrifugal compressor from a manufacturing perspective. In: Proceedings of ASME Turbo Expo. American Society of Mechanical Engineers (ASME), Vancouver, Canada.
- Johnson, M., 1978. Secondary flow in rotating bends. *ASME J. Eng. Power* 100, 553–560.
- Johnston, J., Dean, R.C.J., 1966. Losses in vaneless diffusers of centrifugal compressors and pumps. *ASME J. Eng. Power* 88, 49–60.
- Keane, A., Nair, P., 2005. Computational Approaches for Aerospace Design – The Pursuit of Excellence. John Wiley & Sons Ltd, West Sussex, England.
- Kim, J.H., Choi, J.H., Husain, A., Kim, K.Y., 2010. Multi-objective optimization of a centrifugal compressor impeller through evolutionary algorithms. *IMechE J. Power Energ.* 224, 711–721.
- Kim, J.H., Kim, J.W., Kim, K.Y., 2011. Axial-flow ventilation fan design through multi-objective optimization to enhance aerodynamic performance. *J. Fluids Eng.* 133, 1–12.
- Klassen, H., Wood, A., Schumann, L., 1977. Experimental performance of a 13.65 cm tip diameter tandem bladed sweptback centrifugal compressor designed for a pressure ratio of 6, vol. 1091. National Aeronautics and Space Administration, Scientific and Technical Information Office, Washington, DC Tech. Rep. TP, NASA Technical Report.
- Krain, H., 1981. A study on centrifugal impeller and diffuser flow. *ASME J. Eng. Power* 103, 688–697.
- Lemmon, E., McLinden, M., Huber, M., 2002. NIST reference fluid thermodynamic and transport properties. NIST Standard Reference Database 23; National Institute of Standards and Technology.
- Lettieri, C., Baltadjiev, N., Casey, M., Spakovszky, Z., 2014. Low-flow-coefficient centrifugal compressor design for supercritical CO₂. *J. Turbomach.* 136, 9. doi:10.1115/1.4026322.
- Menter, F.R., 1993. Zonal two-equations k- ω turbulence models for aerodynamic flows. In: Proceedings of the AIAA 24th Fluid Dynamics Conference. AIAA, Orlando, FL, USA, pp. 93–2906.
- Moody, L., 1944. Friction factors for pipe flow. *ASME Trans.* 66, 671–684.
- Munzberg, H., Kurzke, K., 1977. Gasturbinen-Betriebsverhalten und Optimierung. Springer-Verlag, Heidelberg, Germany.
- Olivero, M., Javed, A., Pecnik, R., Colonna, P., van Buijtenen, J., 2011. Study on the tip-clearance effects in the centrifugal compressor of a micro gas turbine by means of numerical simulations. In: Proceedings of International Gas Turbine Congress. Osaka, Japan: IGTC2011-0233.
- Otugen, M., So, R., 1988. Diffuser stall and rotating zones of separated boundary layer. *Exp. Fluids* 6, 521–533.
- Palmer, D., Waterman, W., 1995. Design and development of an advanced two-stage centrifugal compressor. *ASME J. Turbomach.* 117, 205–212.
- Pampreen, R.C., 1973. Small turbomachinery compressor and fan aerodynamics. *ASME J. Eng. Power* 95, 251–270.
- Rodgers, C., Sapiro, L., 1972. Design considerations for high-pressure-ratio centrifugal compressors. In: Proceedings of ASME Gas Turbine and Fluids Engineering Conference. San Francisco, USA. 72-GT-91.
- Rusch, D., Casey, M., 2012. The design space boundaries for high flow capacity centrifugal compressors. In: Proceedings of ASME Turbo Expo. American Society of Mechanical Engineers (ASME), Copenhagen, Denmark.
- Saravanamutto, H., Rogers, G., Cohen, H., 2001. Gas Turbine Theory. Pearson Education Limited, England.
- Schiffmann, J., 2013. Enhanced groove geometry for herringbone grooved journal bearings. *J. Eng. Gas Turbine Power* 135 (10), 102501-1–102501-8. doi:10.1115/1.4025035.
- Schiffmann, J., 2015. Integrated design and multi-objective optimization of a single stage heat-pump turbo-compressor. *J. Turbomach.* 137, 071002. doi:10.1115/1.4029123.
- Schiffmann, J., Favrat, D., 2009. Experimental investigation of a direct driven radial compressor for domestic heat pumps. *Int. J. Refrigeration* 32, 1918–1928. doi:10.1016/j.ijrefrig.2009.07.006.
- Senoo, Y., Kinoshita, Y., 1977. Influence of inlet flow conditions and geometries of centrifugal vaneless diffusers on critical flow angle for reverse flow. *ASME J. Fluids Eng.* 99, 98–102.
- Shibata, T., Yagi, M., Nishida, H., Kobayashi, H., Tanaka, M., 2011. Performance improvement of a centrifugal compressor stage by increasing degree of reaction and optimizing blade loading of a 3d impeller. *ASME J. Turbomach.* 133, 021004.
- Turunen-Saaresti, T., Roytta, P., Honkatukia, J., Backman, J., 2010. Predicting off-design range and performance of refrigeration cycle with two-stage centrifugal compressor and flash intercooler. *Int. J. Refrigeration* 33, 1152–1160. doi:10.1016/j.ijrefrig.2010.04.008.
- van den Braembussche, R., 2006. Optimization of radial impeller geometry. NATO-RTO Educ. Note. RTO-EN-AVT-143 13, 13-1–13-28.
- van den Braembussche, R., 2007. Centrifugal compressors analysis and design. Course Note 192; Von Karman Institute for Fluid Dynamics (VKI).
- Verstraete, T., Alsalihi, Z., den Braembussche, R.A.V., 2010. Multidisciplinary optimization of a radial compressor for micro gas turbine application. *ASME J. Turbomach.* 132, 1–7.
- Walsh, P., Fletcher, P., 2004. Gas Turbine Performance. Blackwell Science Ltd, Oxford, UK.

- Whitfield, A., Baies, N., 1990. Design of Radial Turbomachines. Longman Scientific & Technical, England.
- Yagi, M., Kishibe, T., Shibata, T., Nishida, H., Kobayashi, H., 2008. Performance improvement of centrifugal compressor impellers by optimizing blade-loading distribution. In: Proceedings of ASME Turbo Expo. Berlin, Germany. GT2008-51025.
- Zangeneh, M., Goto, A., Harada, H., 1998. On the design criteria for suppression of secondary flows in centrifugal and mixed flow impellers. *ASME J. Turbomach.* 120, 723–735.
- Zangeneh, M., Amarel, N., Daneshkhah, K., Krain, H., 2011. Optimization of 6.2:1 pressure ratio centrifugal compressor impeller by 3D inverse design. In: Proceedings of ASME Turbo Expo. American Society of Mechanical Engineers (ASME, Vancouver, Canada).
- Zehnder, M., 2004. Efficient air–water heat pumps for high temperature lift residential heating, including oil migration aspects. École Polytechnique Fédérale de Lausanne (EPFL).